The physics of nanowire superconducting single-photon detectors

Renema, J.J.

Chapter 5

Position-Dependent Internal Detection Probability in a Nanowire Superconducting Single-Photon Detector

We probe the local nature of the detection probability in nanowire superconducting single-photon detectors at the nanoscale. By using detector tomography, we demonstrate that the detection probability depends on the distance from the edge of the wire at which a photon is absorbed. We probe this effect with a ∼10 nm resolution. We find that there is qualitative agreement with the diffusion-based vortex crossing model but not with other models.

5.1 Introduction

Nanowire superconducting single-photon detectors typically consist of a 60-100 nm wide, current-carrying, thin, superconducting film [1]. These photodetectors have favourable properties such as high efficiency, low dark count rate and fast reset time [89], and are therefore a key resource for various technologies, such as quantum key distribution [90], interplanetary communication [6] and cancer research [91]. Recently, large steps have been made in the understanding of the internal working mechanism of such detectors.

While the picture is not yet complete, the current understanding of detection events in superconducting single-photon detectors is as follows: an absorbed photon breaks Cooper pairs through an avalanche process, causing a cloud of quasiparticles a few tens of nm in size to form in the superconducting film. This in turn causes the current to be diverted through the

unaffected parts of the wire. If the diverted current is sufficiently strong this causes a magnetic vortex to unbind from the edge of the detector. Under the influence of the Lorentz force, this vortex is pulled across the wire, dissipating enough energy to cause a transition to the normal state, leading to a detection event [17, 24, 25, 28, 33, 34, 72][1]. One unexpected implication of such models is a nanoscale variation of the internal detection efficiency (IDE), i.e. the probability that an absorbed photon is detected: the amount of bias current required to detect a photon of a given energy depends on the position in the cross section of the wire where the photon is absorbed [32, 34].

To observe this effect, one must introduce a variation in the absorption probability as function of position. This can be done by changing polarizations of the light incident on the detector, since light polarized orthogonal to the wire is preferentially absorbed in the center of the wire (see Figure 5.1). However, this introduces a complication: apart from a possible difference in internal efficiency once a photon is absorbed, the two polarizations are also not absorbed with equal efficiency in the first place [10, 11, 12, 13, 92].

In this work, we investigate the local IDE by using a tomographic method to separate the overall absorption probability from the IDE. We find and quantify a polarization-dependent IDE. Our results are consistent with previous qualitative observations [10, 93, 94]. We conclude that the field distribution inside the detector determines the position of the photon absorption event and that the local IDE depends on where the photon is absorbed.

We explore this effect experimentally by measuring the polarization dependence of the internal detection efficiency as a function of wavelength and bias current. From these data we reconstruct the position dependent internal detection efficiency of a 150 nm wide NbN wire with $\sim$10 nm spatial resolution. We compare these data to an ab initio numerical calculation in the context of a diffusion-based vortex crossing model. From the good qualitative agreement with experimental data we conclude that, while this model may require some refinement, it contains the essential microscopic physics of the photon detection event in SSPDs.

5.2 Experiment

To measure the internal detection probability of the detector, we use quantum detector tomography (QDT)[2] [17, 36, 37, 43, 44, 48, 49, 60, 67, 72, 95]. QDT relies on illuminating the detector with a series of known quantum states of light - in our case coherent states - which together function as a probe of the detection statistics. By comparing the response of the detector to different photon numbers in the coherent light state, we can separate the one-photon detection probability p_1 from the overall probability η that a photon is ab-

[1] See Chapter 4.
[2] See Chapter 2.

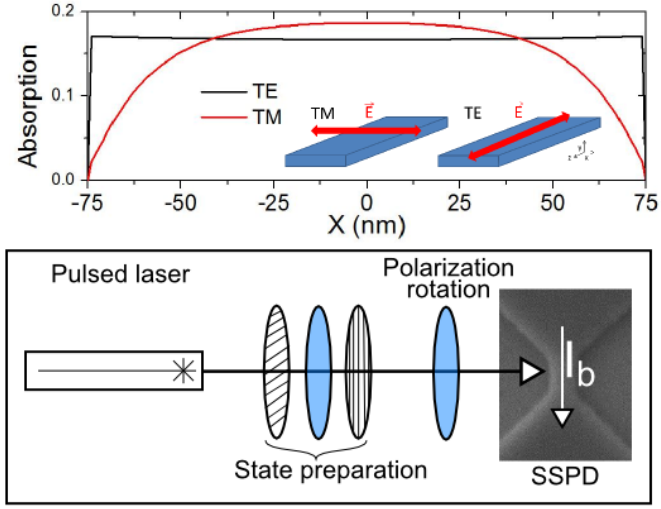

Figure 5.1: Sketch of our experiment. *Top:* Absorption as a function of position in the wire for parallel (TE) and perpendicular (TM) polarizations, calculated with an FDTD method (see text). *Inset*: Sketch showing the TE and TM polarizations. The red arrow represents the polarization of the electric field. *Bottom*: Experimental setup. Our laser pulses are tuned in intensity by a variable attenuator consisting of two crossed polarizers and a $\lambda/2$ wave plate. Polarization is set by an additional $\lambda/2$ wave plate. The image is a SEM micrograph of a detector nominally identical to the one used in this experiment.

sorbed[3]. From the fact that η is almost independent of bias current [67] and that it corresponds to the area of our detector, we identify p_1 with the IDE.

We perform our experiments on a 100 nm long, 150 nm wide NbN bridge patterned on a 5 nm-thick NbN sputtered on a GaAs substrate [47]. We read out the detector with the usual measurement setup based on a bias-tee to separate high-frequency detection pulses from the DC bias current, followed by a series of RF amplifiers and a pulse counter. At each combination of bias current, photon energy and polarization, we record the detector count rate as a function of input intensity. Our probe states were prepared by a broadband pulsed laser (Fianium, repetition rate 20 MHz) out of which we select a narrow wavelength band with dielectric filters[4]. We prepare the desired intensity and polarization by first attenuating the light with a combination of two crossed polarizers and a half-wave plate, and then setting the polarization with an additional wave plate (see Figure 5.1)[5].

[3]For more information, see Appendix I.

[4]For a more extensive description of our setup, see Chapter 4, Appendix I.

[5]While in principle it is possible to achieve the desired combination of polarizations

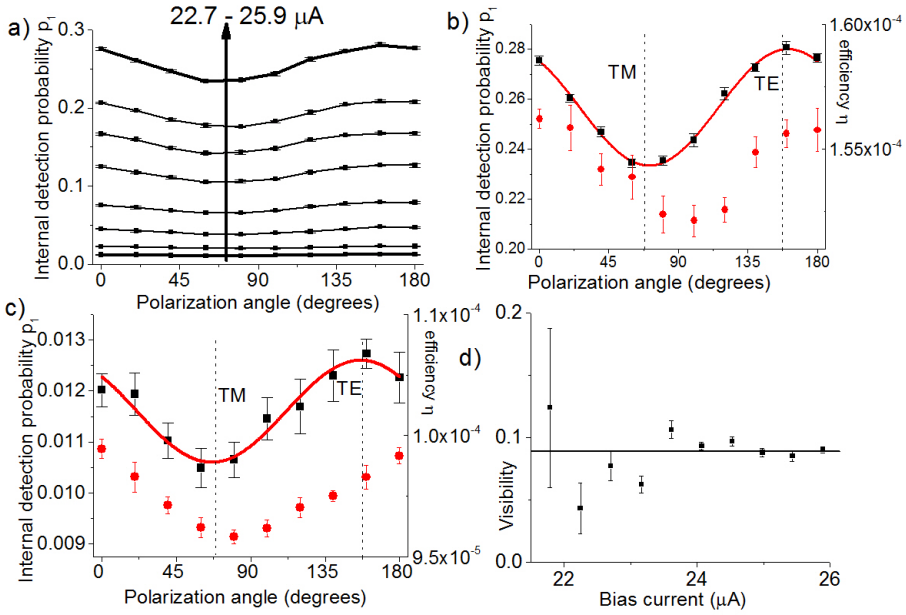

Figure 5.2: Experimental results on the polarization dependence of the internal detection probability at an excitation wavelength of 1500 nm. *a)* Internal detection probability p_1 as a function of input polarization, for different bias currents (0.5 μA apart). *b),c)* Zoom-ins on two typical experimental results (marked in thicker lines in *a)*) at different bias currents. We plot the internal detection probability p_1 (squares) as well as the absorption efficiency η (circles). The red lines are sine fits with a fixed period of 180 degrees. *d)* Visibilty of the observed oscillation in p_1 as a function of bias current. We find that our results are consistent with a constant visibility of $V = 0.09$.

5.3 Results

Figure 5.2 shows that the internal detection probability of our device is dependent on polarization. We plot the internal detection efficiency p_1 as a function of the polarization of light with $\lambda = 1500$ nm. Each curve represents a different bias current, in steps of 0.5 μA. We find that over the current range where our experiment has sufficient signal to noise ratio, the visibility $V = (p_{max} - p_{min})/(p_{max} + p_{min})$ is independent of bias current. For this wavelength, we find $V = 0.09$. The error bars in Figure 5.2 are derived from a series of repeated experiments which are analyzed independently, for which we plot the mean and standard deviation[6].

Our experiments show that the internal detection efficiency and external detection efficiency oscilate in phase when the polarization is rotated, with a minimum at TM polarization and a maximum at TE polarization. This demonstrates that absorption of TM-polarized photons is less likely to result in a detection. This polarization is absorbed in the middle of the wire. Our result therefore confirms the preliminary result of Anant *et al.* [10]: at a given bias current, the edges of the detector are therefore more efficiently photodetecting than the center of the wire.

In order to quantify the variations in local IDE we must compute the IDE as a function of polarization. We do this by multiplying the local optical absorption probability with the local IDE. We do this for each wavelength at which we measure the polarization-dependent detection probability.

Our strategy is to take the absorption profiles as given - since they are well studied - and to take the internal detection efficiency (IDE) profile as a free parameter and fit it to our experimental data. The rest of this chapter is structured as follows: first, we will describe the computation of the two profiles, resulting in a fit to our experimental data. Then, we will compare the resulting internal detection efficiency profile to one that we calculated from an ab initio theory.

To calculate the absorption distributions, we perform a series of numerical simulations at the wavelengths at which we conducted our experiments of the polarization-dependent absorption in the detector structure using a finite-difference time domain (FDTD) method (RSOFT Fullwave). We consider a 2D model of a 150 nm wide, 5 nm thick NbN wire on a semi-infinite GaAs substrate and an 80 nm thick HSQ layer on top of the NbN wire. The refractive index of NbN deposited film on GaAs is derived from spectroscopic ellipsometry measurements [96]. In these calculations we neglect the effect of the tapered parts of the bridge because they have little influence on the absorption in the central, photodetecting section[7]. In Figure 5.1, the result

---

and intensities using two independently rotating polarizers, we found that the effects of wedge in the polarizers preclude this solution.

[6] We will analyze the change in linear efficiency from $\eta = 1.6 * 10^{-4}$ to $\eta = 1.1 * 10^{-4}$ in Chapter 7.

[7] See Appendix I for details.

of this calculation is shown for $\lambda = 1500$ nm.

For the internal detection probability, we use the fact that the energy-current relation was measured to be of the form $I_{th} = I_0 - \gamma E$, [28, 17, 72] where I_{th} is the threshold current (i.e. the current where the detection efficiency is equal to some reference value), I_0 is the reference current[8], E is the photon energy and γ is an experimental ratio which describes the interchange between bias current and photon energy. We postulate that this relation holds microscopically, i.e. $j_{th}(x) = j_0 - \gamma'(x)E$. Moreover, we must posit a relation between threshold current and detection probability. For this, we postulate the relation $P(x) = \min\{1, \exp(j_b - j_{th})/j^\star\}$, with $P(x)$ the local detection probability, j_b the bias current density,[9] and $j^\star = 0.9$ GA/m^2 the low-detection probability scale which can be read off from the experimental data when converted to a bias current. This relation is motivated by the idea that at $P(x) < 1$ the detection process consists of tunneling through the energy barrier binding the vortices to the edge of the wire [23, 33]. With this set of assumptions, we are able to compute the polarization visibility for different wavelengths, with the $\gamma'(x)$ profile specified at 10 nm intervals as fit parameters.

Figure 5.3 shows the calculated and measured visibility of the polarization-dependent internal efficiency as a function of wavelength. We find that at long wavelengths there is a greater difference between the measured IDE for the two polarizations. The line in Figure 5.3 shows the result of our fit of the internal detection profile to the data. From the local IDE and the optical absorption probability, we compute the overall IDE. We find that we are able to reproduce the observed internal efficiencies with our fit. The left inset of Figure 5.3 shows the dependence of the polarization-dependent IDE visibility on current. We find that theoretically, the IDE visibility is independent of current, which is reasonable agreement with our experimental data.

The right inset shows the overall value of the single-photon internal detection efficiency, integrated across the wire. We observe that our curve predicts the right current for the roll-off at low detection probabilities, and that it reproduces the slow saturation of the detector at high currents. In this regime, parts of the detector are fully photodetecting, while other parts are still in a fluctuation-assisted regime [35]. The variations between the experimental data and the calculated values are less than a factor of 2. We stress that the two insets of Figure 5.3 are direct results of the internal detection efficiency profile inferred from the polarization measurements. We therefore conclude that our proposed internal detection probability profile is consistent with all of the observed properties of our detector.

[8] see Chapter 4.

[9] Throughout this Chapter, we assume homogeneous current flow, so the relation $j = I_b/(wd)$ holds.

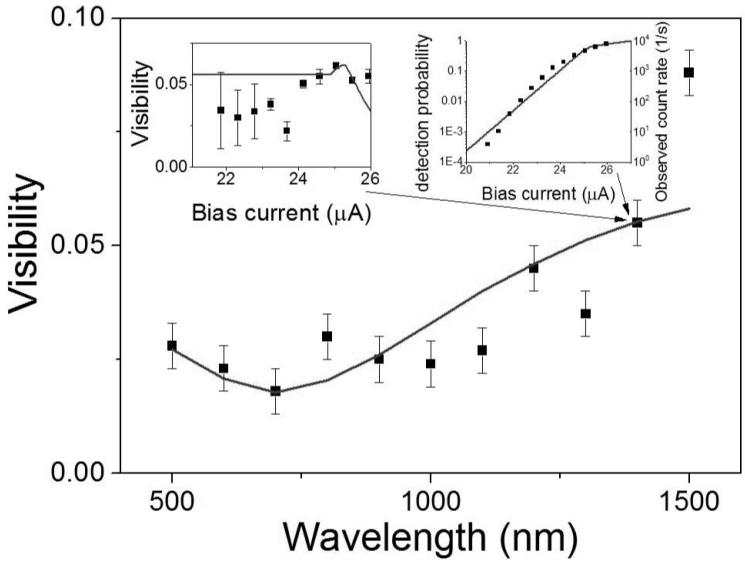

Figure 5.3: Wavelength-dependent visibility of the internal detection efficiency (p_1). The black squares show the experimental data. The line shows a fit of the internal efficiency profile, based on the diffusion-based vortex crossing model. *Left inset:* Measured (squares) and computed (line) visibility of the polarization-dependent oscilation as a function of bias current. *Right inset:* Observed (squares) and computed (line) values the integrated single-photon internal detection probability p_1.

5.4 Comparison to Theory

Figure 5.4 shows the internal threshold current profile which comes from the fit to the wavelength-dependent polarization visibility data, for a wavelength of 1000 nm (see also Figure 5.3). For comparison with other experiments, we plot the overall bias current required to make a particular part of the wire fully photodetecting. We estimate the systematic error on the threshold current that is induced by uncertainty in the calculation of the optical absorption profiles[10], shown in Figure 5.4 as a grey band around our data, which is particularly prominent around 50 nm. We find that this effect is negligible compared to the statistical error. Moreover, it shows an independent, ab initio calculation of the threshold current based on the model described below. We find reasonably good agreement between our observed experimental results and the theoretical values. From this, we conclude that our model is sufficiently detailed to model the detection process in SSPDs.

Our ab initio calculations of the position-dependent detection probability are based on a numerical model[11] that allows one to determine the threshold current for the detection of an absorbed photon of a given wavelength [28] and a recently proposed extension [32]. Based on a simple model of quasiparticle generation and diffusion, we determine the local reduction of the order parameter after the photon has been absorbed. Solving the continuity equation for the applied bias current for this inhomogeneous situation, we are then able to calculate the time evolution of the vortex-entry barrier. The minimum bias current that leads to a vanishing barrier height is defined as the threshold current for photon detection, as this will unavoidably lead to a vortex entering the strip. Its subsequent movement across the strip under the action of the bias current then leads to the formation of the initial normal conducting domain triggering the detection event.

We compute the threshold current for various photon energies and absorption positions across the strip and we find a linear relation between photon energy and threshold current for each position. This vindicates the assumption that the linear relation between current and photon energy holds on a microscopic level[12].

Our ab initio calculation gives a physical explanation for the enhanced efficiency at the edges of the wire in terms of our microscopic model. Comparing a photon absorption in the center of the wire to one at the edge, there are two differences. First, for an absorption event at the edge, the current density at the edge of the wire is reduced, due to the reduction in the number of superconducting electrons n_s. However, this is more than compensated by the reduction of the vortex self-energy, which is proportional to n_s. Vortices enter more easily when the superconductivity is weakened at their entry point, and that makes the detector more efficient at the edges.

[10] See Appendix I for details.
[11] These simulations were performed by Andreas Engel at the University of Zurich.
[12] See Appendix I for details.

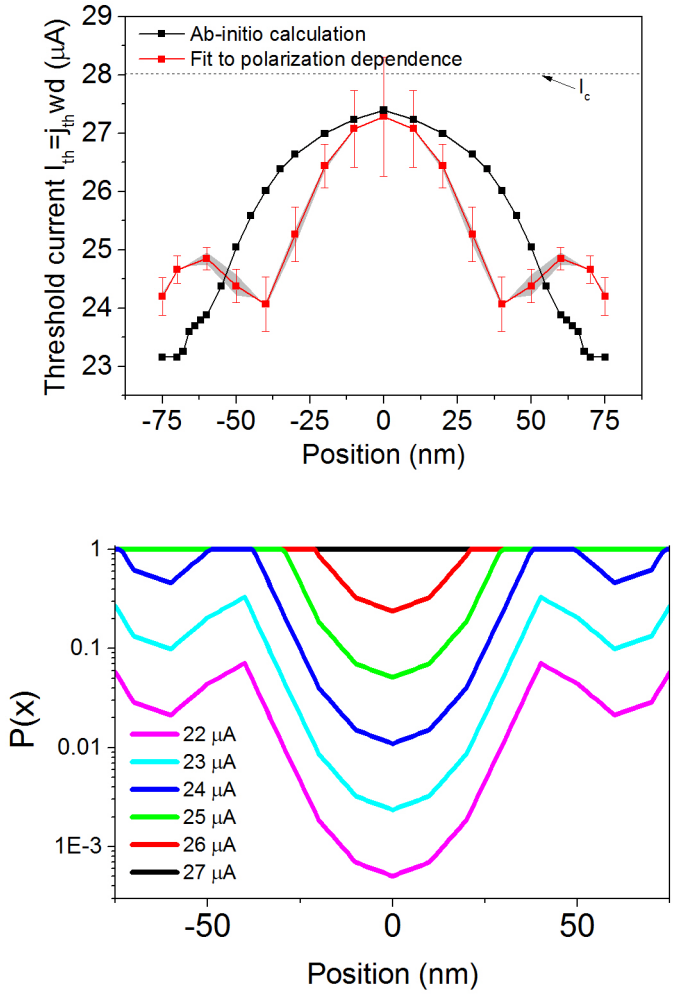

Figure 5.4: *Top panel:* Threshold current as a function of position across the detector, for our fit and our ab initio calculation, for a wavelength of λ = 1000 nm. The red curve shows the fit from Figure 5.3, the black curve shows our ab initio calculation. The grey band shows the systematic error coming from the uncertainty in the film thickness. The dashed line indicates the critical current. *Bottom panel:* Calculated position-dependent detection probability density as a function of bias current (1 μA intervals). At a bias current where the edges of the wire are fully photodetecting, the detection probability in the middle of the wire is less than 1%.

The bottom panel of Figure 5.4 shows the consequences of the variation of the internal detection efficiency, evaluated for a photon with wavelength $\lambda = 1000$ nm. We plot the detection probability as a function of position for different bias currents. The effect of the position-dependent detection efficiency is quite strong: for a current of 25 μA, photons absorbed at the very edge of the detector have 100% probability of causing a detection event, whereas photons absorbed at the center of the wire have only 3% probability.

5.5 Discussion and Conclusion

We note that there is some disagreement in literature about the shape of the internal detection probability curve. The alternative model of Zotova *et al.* [34], which is based on the Ginzburg-Landau formalism, naturally takes into account vortex entry. However, it disregards quasiparticle diffusion and implements a hotspot with hard boundaries. The results from this model disagree qualitatively with our experimental results: there, a W-shaped threshold current profile is predicted, with threshold currents at the edges almost as high as in the center of the wire. The discrepancy between their model and ours occurs precisely at the point where their 'hard' hotspot touches the edge of the wire. We speculate that both models, if refined more, will likely converge in their predictions.

In conclusion, we have demonstrated via detector tomography that the internal detection probability of an SSPD depends on the distance from the edge of the nanowire at which the photon is absorbed. We have probed this effect with a resolution of approximately 10 nm. This effect occurs in addition to the well-known effect that photons of parallel polarization are more efficiently absorbed in the wire. From the wavelength dependence of this effect we have derived a spatial profile for the local internal detection efficiency, which is in good agreement with theoretical calculations done in the context of the diffusion-based vortex crossing model. From this, we conclude that this model contains the essential features for a complete microscopic picture of the detection model in SSPDs. These results pave the way for quantitative theoretical results on the detection mechanism in SSPDs.

5.i Appendix: Supplementary Material

5.i.1 Quantum Detector Tomography

The purpose of this section is to review quantum detector tomograpy as a technique, and to demonstrate that we can separate the change in internal detection probability associated with a change in polarization from the change in overall efficiency. This section consists of three parts. First, we review the basics of quantum detector tomography. Then, we investigate the input power dynamic range requirements of our experiment. Lastly, we demonstrate that our experiment is accurate enough that we can reject the alternate hypotheses that our results are entirely attributable to a change in only either the internal or external detection efficiency.

5.i.1.1 Tomography Basics[13]

The goal of quantum detector tomography is to find the photodetection statistics of an unknown detector in the number state basis, i.e. to find the probability of a particular detection outcome given that n photons are incident on the detector. To probe these statistics, a collection of known quantum states of light is used. The detector is probed sufficiently many times with each state to accurately determine the probability of each possible experimental outcome (i.e. a detection event) for each input state. Since the probability distribution of photons in the states is known and the probability of each outcome has been measured, it is possible to determine the probability of each outcome given a certain number of photons.

In experimental practice, it is convenient to use the coherent states for this, which have a Poisson-distributed probability of photon numbers: $\Pi_i(N) = e^{-N}N^i/i!$, where N is the mean photon number, which can be determined clasically, and i indexes the Fock states. These states are readily produced by a laser, and the mean photon number can be adjusted by attenuation, giving straightforward access to a sufficiently large set of quantum states. We denote the probability of the k-th experimental outcome to the j-th test state $R_k(N_j)$. The probability for i photons to produce the k-th experimental outcome $p_{k,i}$, which is the desired quantity, can then be found by solving the matrix equation:

$$R_k(N_j) = \Pi_i(N_j)p_{k,i}. \tag{5.1}$$

An SSPD has only two outcomes, a detection event (click) or the lack of a detection event (no click), and because overall probabilities must sum to 1, it is sufficient to consider only one of these. In Chapter 2, we modified equation 5.1 to make it usable in the case where only a very small fraction of the photons participates in the detection process. We did this by introducing

[13] See also Chapter 2.

a separate quantity η which describes the overall linear efficiency of the detection process. We arrive at:

$$R_{click}(N) = 1 - e^{-\eta N} \sum_{n=0}^{n<n_{max}} (1 - p_n) \frac{(\eta N)^n}{n!}, \tag{5.2}$$

where R_{click} is the observed detection rate as a function of input power, η is the overall efficiency with which photons participate in the detection process, and p_n represents the probability that the n-photon absorption event results in a photodetection event.

To fix the additional degree of freedom introduced by the linear efficiency, we must introduce an additional assumption. The essential assumption behind our modified version of quantum detector tomography is that there is some unknown but large photon number for which the count rate tends to a known, constant value[14], in our case $R_{click}(N \to \infty) = 1$. For an SSPD, the assumption is well justified by the fact that high-energy excitations are known to be more efficiently detected than low-energy ones. It is therefore not unreasonable to assume that we have $p_n = 1$ for sufficiently large n_{max}. At these powers, we can fix η, and find the nonunity $p_{n<n_{max}}$ from the low count rate values.

The resulting procedure is illustrated in Figure 5.5, where we plot a data set from Chapter 2 to demonstrate the procedure. At high powers, we assume $p_n = 1$, which enables us to fix η. At lower light powers this discription becomes inadequate, and we must adjust p_n to fit our data. The threshold value n_{max} for which $p_{n \geq n_{max}} = 1$ can be found via model selection. In the present experiment, we are working in the regime where only nonlinearities at the single-photon level play a role, so $n_{max} = 2$ throughout. The only exception is the multiphoton experiment reported on in Section 5.6.2.

5.i.1.2 Dynamic Range

From the discussion above, it is clear that sufficient dynamic range in input powers is the essential requirement for quantum detector tomography. In order for the procedure to work, sufficiently high powers must be taken into account to obtain an adequate measurement of the saturation behaviour of the detector. In order to ascertain whether this is the case in our experiment, we perform the following numerical procedure: we carry out detector tomography on our entire ensamble of data points. Then, we remove the data point at highest power, perform tomography again, and repeat this procedure. If we have sufficient dynamic range in our experiment, we expect to find that our results are independent of the specific choice of probe states.

[14] We note that in Chapter 2 [67], we claimed that the requirement is saturation, i.e. $R_{N\to\infty} = 1$. While this is by far the most natural case, in principle it is possible for a detector to have $R_{N\to\infty} \neq 1$, for example the one-element detection probability of a multi-element detector, which has $R_{N\to\infty} = 0$. Equation 5.1 can be trivially rewritten to accomodate this case.

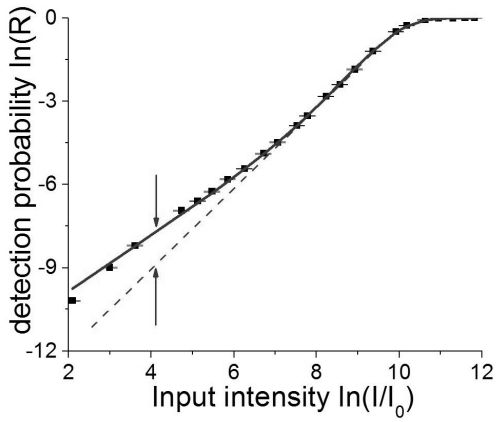

Figure 5.5: Sketch of quantum detector tomography (data taken from Chapter 2). We measure the response of an SSPD at various input powers. The solid line shows the fit to equation 5.2 for this data set. The dashed line shows the low-power extrapolation from the high-power data.

Figure 5.6 shows that this is indeed the case. We plot the internal detection probability p_1 as a function of the dynamic range in our probe states, for one data set of our experiment (1500 nm). We find that for dynamic ranges > 150, our result is independent of which subset of our data we choose. This data set is representative of our full set of experimental results; we typically find values between 100 and 300 for the minimum dynamic range requirement. This demonstrates the robustness of our result.

5.i.1.3 Constant p_1 and Constant η

Lastly, we demonstrate that we are able to reject the alternative hypotheses that our experimental results can be explained by only a polarization-induced modulation in either p_1 or η. To ascertain this, we perform the following analysis: at each set of experimental settings (input wavelength, input power, bias current, polarization) we record a series of independent measurements. Then, we process these measurements separately. This gives us a measure of the statistical spread of our results.

In Figure 5.7, we plot the result of this procedure for one data set at 826 nm. Each set of symbols of the same colour represents ten realizations of the same experimental setting, and the spread within each colour is therefore a measure of the statistical spread in our experiment. We find that there is negative covariance between internal and external efficiency. However, the spread which this covariance causes is much smaller than the typical polarization-induced shift in either p_1 or η. The two dashed lines indicate the

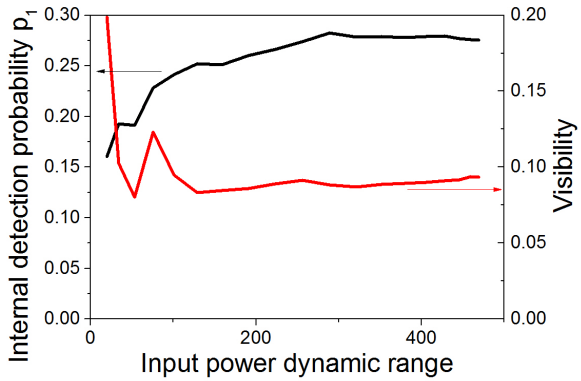

Figure 5.6: Quantum detector tomography at different dynamic ranges in the input power. We plot the internal detection probability as a function of bias current for a given polarization at fixed bias current, at an excitation wavelength of 1500 nm. The red curve shows the observed visibility for the data set to which this polarization belongs as a function of dynamic range. We find that for a dynamic range > 150, the observed visibility is independent of the chosen range. This indicates that at sufficient dynamic range, our results are independent of the choice of input powers.

alternative hypotheses in which only either p_1 or η is polarization-dependent. It can be seen that a large part of our data is far away from these two lines. From this, we conclude that both internal and external effects are necessary to explain our measurements.

5.i.2 Multiphoton Polarization Effects

Detection events in SSPDs can also occur via multiphoton excitation [1, 67]. We performed an experiment at 826 nm where we illuminate the detector with sufficient power to cause two-photon processes at lower bias current. Figure 5.8 shows the results of this experiment. We find that also for multiphoton processes, the internal detection efficiency is position-dependent. We find that the visibility is a factor 2-3 higher for the 2-photon excitations than for the single-photon excitations.

We can offer two partial explanations for the enhanced visibility. First, we demonstrated in Chapter 2 that multiphoton excitations are equivalent - at least in their energy-current dependence - to single-photon excitations of the same energy. From our simulations of the internal detection efficiency, we find that the difference in threshold current between the edges of the wire and the center decreases with increasing photon energy. We therefore expect two 826 nm photons to respond similarly to a single 413 nm photon

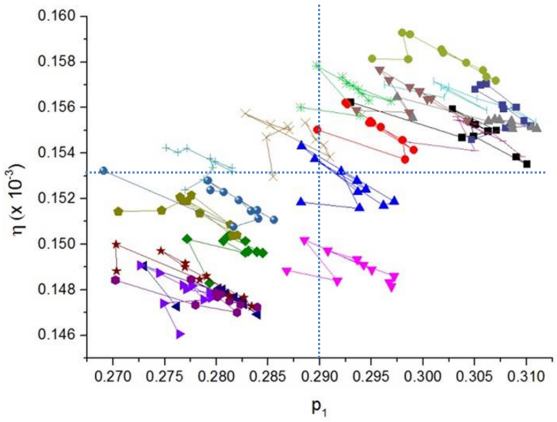

Figure 5.7: Experimental test of the statistical relevance of our result. Each set of symbols represents a single experimental setting, the spread between them is a measure of the statistical uncertainty in our experiment. There is a negative covariance between p_1 and η within each experimental setting, as expected.

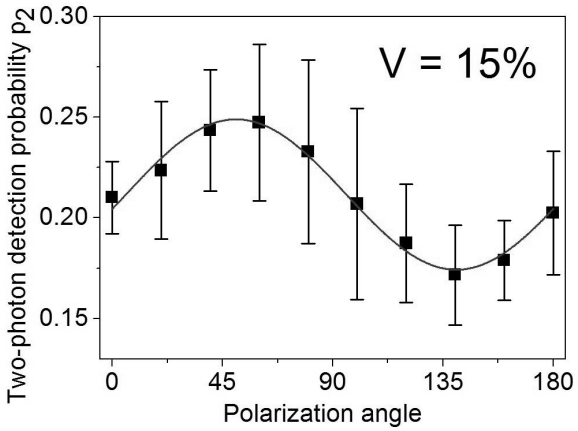

Figure 5.8: Multiphoton polarization-dependent absorption. We plot the two-photon detection probability p_2 as a function of polarization angle. The line shows a sine fit with a fixed period of 180 degrees to the data.

and experience a greater difference in detection efficiency. A second effect is that, qualitatively, we expect the two-photon absorption probability to be more sharply peaked at the edges of the wire. However, a full quantitative investigation of this multiphoton effect would involve computation of the internal detection efficiency for each possible two-photon absorption scenario, which is beyond the scope of the present work.

5.i.3 Numerical Detection Model

The simulation of the quasiparticle distribution after the absorption of a photon is based on the model described in [28]. Here, we will repeat the main features and assumptions of this model. It is assumed that the photon excites one electron with energy hc/λ. This electron moves in the film with a diffusion constant D_e. It thermalizes via inelastic scattering with other electrons/Cooper-pairs and the lattice. Neglecting details of this thermalization process, an exponential increase of excess quasiparticles is assumed with a time constant τ_{qp} and an overall efficiency ς [15]. The excess quasiparticles themselves are also subject to diffusion with a temperature dependent diffusion constant $D_{qp} < D_e$ and eventually recombine to form Cooper-pairs on a time-scale $\tau_r \gg \tau_{qp}$. This can be described by the following coupled differential equations [28]:

$$\frac{\partial C_e(r,t)}{\partial t} = D_e \nabla^2 C_e(r,t) \tag{5.3}$$

$$\frac{\partial C_{qp}(r,t)}{\partial t} = D_{qp}\nabla^2 C_{qp}(r,t) - C_{qp}/\tau_r + \frac{\varsigma h\nu}{\Delta \tau_{qp}} \exp(-t/\tau_{qp}) C_e(r,t), \tag{5.4}$$

with Δ the superconducting gap, $C_e(r,t)$ the probability density to find the excited electron at position r at time t after photon absorption and $C_{qp}(r,t)$ the quasiparticle density.

An estimation of the Ginzburg-Landau relaxation time results in $\tau_{gp} \ll 1$ ps. Therefore, we assume the current redistribution due to the spatial variation of the density of superconducting electrons $n_{se} - C_{qp}(r,t)$ to be instantaneous on time scales > 1 ps. To obtain a more realistic current-distribution than in [28], we now apply the relation that the velocity of superconducting electrons can be calculated from the gradient of the phase of the superconducting condensate [32]:

$$v_S = \frac{\hbar}{m}\nabla\varphi, \tag{5.5}$$

and the current density then becomes

$$j_s = -en_{se}\frac{\hbar}{m}\nabla\varphi. \tag{5.6}$$

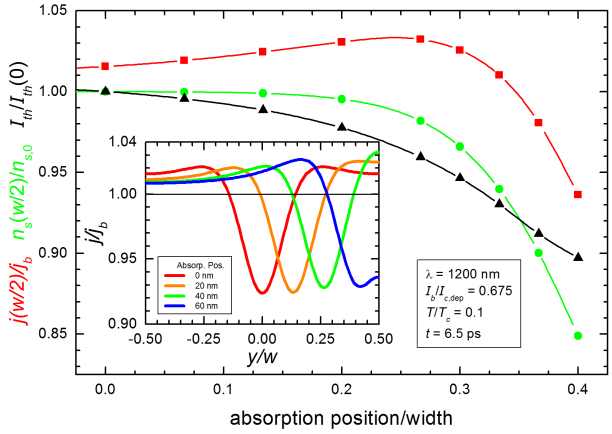

Figure 5.9: Variation of reduced current density at the edge $j_{(w/2)}/j_b$, normalized density of superconducting electrons $n_{s(w/2)}/n_{s,0}$, and rescaled threshold current for photon detection as a function of the distance of the photon absorption position from the center of the wire. The variation of the threshold current near the center of the wire is dominated by the variation of the current density at the edge. For absorption events closer to the edge the reduction of the density of superconducting electrons becomes the dominating effect. In the inset we show the variation of the current density across the wire for different absorption positions.

and we have to solve the continuity equation:

$$\nabla \cdot (-en_{se}\nabla\varphi) = 0, \tag{5.7}$$

where we use the previously calculated quasiparticle distribution to obtain n_{se}. Additionally, we take into account that the density of superconducting electrons depends on the velocity v_s [97].

$$n_{se} \propto 1 - (v_s/v_c)^2/3, \tag{5.8}$$

with v_c the critical velocity at the critical-current density j_c. Thus equation 5.7 becomes nonlinear. Once we know the current distribution, the potential energy experienced by a vortex be can calculated as suggested in [29]. More details about the refined numerical model can be found in [32].

In the inset of Figure 5.9 we plot reduced current densities j/j_b across the strip for some absorption positions. At first, current densities increase with decreasing distance of the absorption position to the near edge. If the distance becomes less than 20 nm to the edge the current density near the edge is reduced, eventually below the equilibrium bias current-density j_b.

In the main graph of Figure 5.9 the reduced current density at the edge $j_{(w/2)}/j_b$ is plotted as a function of absorption position, together with the

density of superconducting electrons at the edge $n_{s(w/2)}$ normalized to their equilibrium density $n_{s,0}$, and the threshold current scaled by the threshold current for absorption in the center $I_{th}/I_{th(0)}$. For absorption events near the center, the variation of the threshold current is mostly determined by the variation of the current density at the edge, since the density of superconducting electrons at the edge remains approximately constant. At close distances to the edge n_s is significantly reduced at the edge. This is the reason for a reduced current density at the edge, but additionally leads to a reduction of the vortex self-energy which is proportional to n_s. This second effect is stronger than the effect of the reduced current density and as a result we obtain a monotonic reduction of the threshold current for vortex entry as a function of the distance from the strip center.

We define the threshold current as that value of the bias current for which the maximum potential energy for a vortex becomes zero. In this case we expect an internal detection efficiency equal to one. With this criterion, we obtain the energy dependence of the threshold current as a function of position, which is plotted in Figure 5.10. The vortex-entry current without photon absorption is also indicated by the horizontal line. This curve is symmetric with respect to the center line of the wire due to the symmetry between vortices and antivortices in zero applied magnetic field. There is a significant reduction of the threshold current for photons absorbed near the edge of around 10% as compared to the center of the wire. We would like to point out that for each position in the wire we find a linear relation between threshold current and photon energy, consistent with previous experimental results [18] reported in Chapters 3 and 4.

As the photon energy increases and as absorption occurs closer to the edge, the relation between the density of superconducting electrons and the current distribution (equations 5.7 and 5.8) becomes more nonlinear. For absorptions very close to the edge, the nonlinear solver produces systematic errors. For all wavelengths, we do not calculate the detection current for absorption sites closer than one coherence length to the edge of the wire. For short wavelengths, the area in which this occurs increases, to approximately 12 nm from each edge at 800 nm. In our calculations, we assume that the detection current this close to the edge of the wire is weakly dependent on the absorption position and set it constant, with a value equal to the threshold current in the point closest to the edge that we can still reliably compute.

In our experiment, we are operating below this threshold current. To convert the threshold current into a local detection probability, we assume a functional dependence of the form $p(I_b) = exp((j_{th} - j_b)/j^\star)$, where $j^\star = 0.9$ GA is an experimentally determined scaling current. In this way, we obtain the variation of the internal detection efficiency for a given bias current as shown in the inset of Figure 5.4

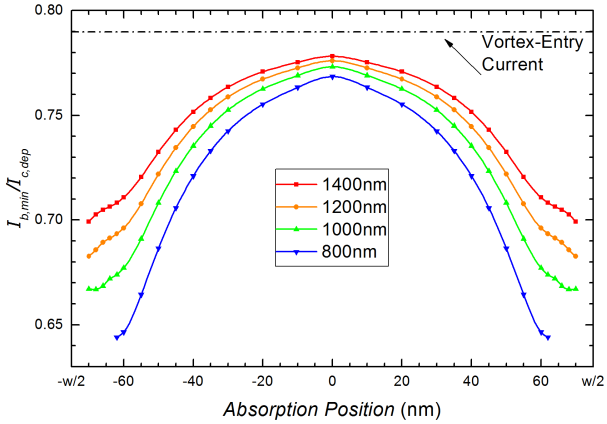

Figure 5.10: Calculated threshold current as a function of the distance of the photon absorption position from the center of the wire for different photon wavelengths. The relative reduction of the threshold current for absorption near the edge compared to absorption in the center increases with increasing photon energy for the energy range considered in this study.

5.i.4 Absorption Calculations

In this section, we demonstrate two things: first, that the absorption in the NbN wire is well approximated by considering only a 2D cross-section, i.e. that the effect from the tapers of the bridge used in our experiment is small. Second, we show that the uncertainty in the dielectric constant of our film does not strongly affect the overall absorption profiles.

We calculate the absorption of the detector for both polarizations using a finite-difference-time-domain (FDTD) programme (RSOFT Fullwave). To test whether the effect of the taper is prominent, we perform a 3D simulation at a wavelength of $\lambda = 1500$ nm, including the tapered parts and the central wire, which is 150 nm wide, 200 nm long and 5 nm thick. The results of this calculation are shown in Figure 1. The top plots of Figure 5.11 (a) and (b) are 1D absorption distributions across the wire from the center (z = 0 nm) to the ends of the wire, extracted from the 3D simulations. For the case of both TE and TM, the absorption distributions across the wire have roughly the same shape, irrespective of the position along the wire at which they are taken.

We compare these 3D results with a 2D simulation, in which the detector is modeled as an infinite wire. The bottom panels of Figure 5.11 (a) and (b) show the comparison of 2D (solid) and 3D (dashed) simulation, where the 3D absorption curve is the average of the absorption curves at different z positions shown in the top part of Figure 5.11. Because we are only interested in relative differences within each absorption profile, we normalized the 2D

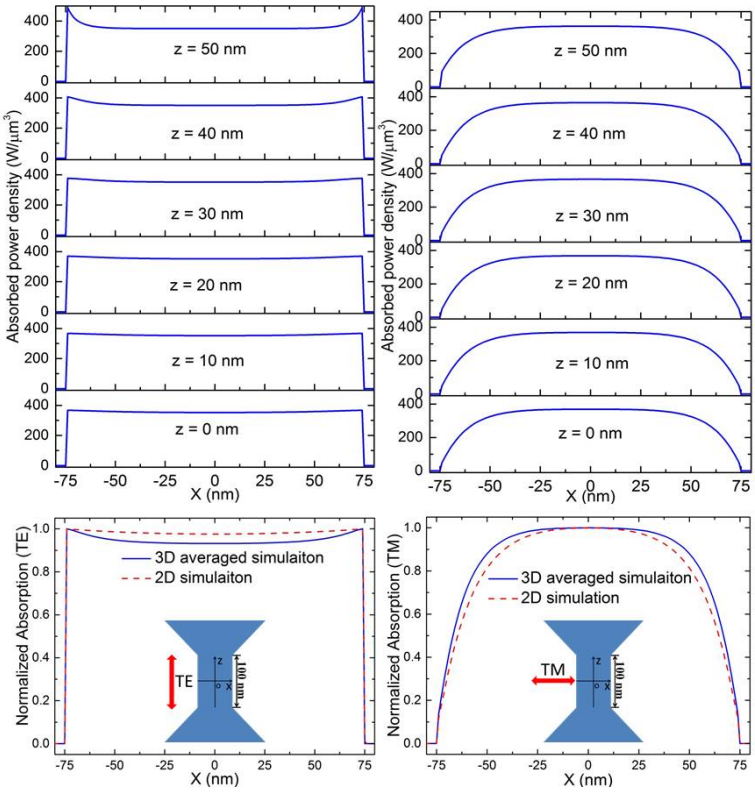

Figure 5.11: Absorption distribution in 2D and 3D, computed at a wavelength of 1500 nm for TE (left) and TM (right). In each subfigure, the top panel shows the 1D absorption density across the wire at different positions on z axis, and the bottom panel shows the averaged absorption (dashed line) of six curves on the top, as well as the result of the 2D simulation, which does not consider the tapered parts.

and the averaged 3D curves to their maximal values individually. For both the TE and TM case there is little difference between the 3D and 2D absorption profiles, which means that we are justified in using the computationally efficient 2D simulations in our main text.

The dielectric constant of NbN ϵ_{NbN} used throughout these calculations is obtained from ellipsometry measurements. If we calculate ϵ_{NbN} from these measurements, the result will depend on the assumed thickness of the film. To assess the implications of this effect, our strategy is therefore to re-calculate ϵ for different thicknesses, and observe the effect on the absorption profiles. In [96], the thickness of the film was estimated to be 4.9nm $\pm$ 0.1nm. We assume a more conservative error bar $\pm$ 0.3nm on the thickness, based on the thickness of a single atomic layer. Then we compute

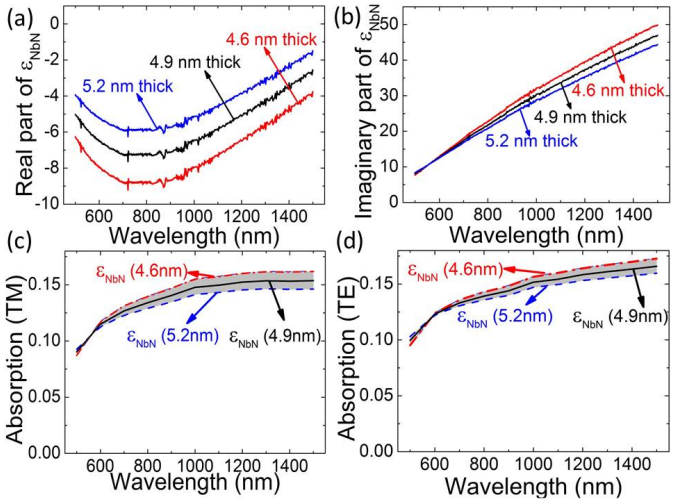

Figure 5.12: Dielectric constant of NbN obtained by considering potential errors in the thickness of the NbN film. (a) and (b) show the real and imaginary part of ϵ_{NbN}. (c) and (d) show the absorption of the 2D NbN wire with the three sets of dielectric constant of NbN, for TM and TE respectively.

the related epsilon $\epsilon_{\mathrm{NbN(4.6\ nm)}}$ and $\epsilon_{\mathrm{NbN(5.2\ nm)}}$ for thickness of 4.6 nm and 5.2 nm. These are shown in Figure 5.12 (a) (real part) and (b) (imaginary part). Throughout Figure 5.12, red and blue lines indicate $\epsilon_{\mathrm{NbN(4.6\ nm)}}$ and $\epsilon_{\mathrm{NbN(5.2\ nm)}}$ respectively. Then, we compute the absorption using these two new sets of dielectric constants. We obtain the total absorption in the NbN wire as a function of wavelength, which is shown in Figure 5.12 (c) for TE and in Fig 5.12 (d) for TM. For most wavelengths (600nm – 1500 nm), $\epsilon_{\mathrm{NbN(4.6\ nm)}}$ causes higher absorption, which is due to its larger imaginary part of dielectric constant at small thickness (4.6 nm).

Variations in ϵ_{NbN} also affect the distribution of absorption across the wire. To investigate this, we calculate the position-dependent absorption with the three sets of ϵ_{NbN} for TE and TM polarization. The inset of Figure 5.13 shows these, for three representative wavelengths of 500nm (a), 1000nm (b) and 1500nm (c). We plot the ratio between TE and TM, since this is ultimately the quantity of interest. In Figure 5.13, the ratios of the TE absorption over the TM absorption for each of the three wavelengths are shown. The small variations indicate that any potential systematic error in the dielectric constant due to a different thickness of the film does not significantly influence our results in the main text.

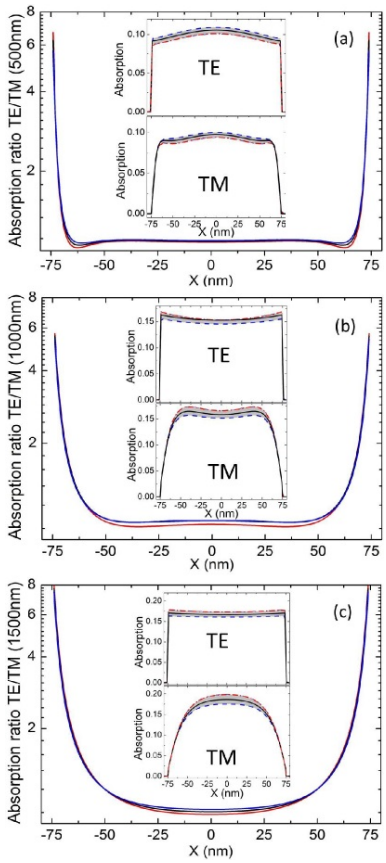

Figure 5.13: Position-dependent absorption ratio TE / TM at wavelengths of 500 nm (a), 1000 nm (b) and 1500 nm (c). In each sub-figure, three dielectric constants (red for $\epsilon_{\mathrm{NbN(4.6\ nm)}}$, black for $\epsilon_{\mathrm{NbN(4.9\ nm)}}$ and blue for $\epsilon_{\mathrm{NbN(5.2\ nm)}}$) are plotted, corresponding to three different thicknesses of the film. The insets show the absorption distributions for TE and TM illumination individually.

5.i.5 Computation of Polarization-Dependent Visibility

In this section, we outline the algorithm which we use for computing the visibility of the polarization-dependent oscilation in p_1 from a given microscopic energy-current relation $\gamma'(x)$.

- Interpolate $\gamma'(x)$ on a 1 nm grid, from the points at which it is given. We assume mirror symmetry around the point $x = 0$.
- Normalize each pair of absorption profiles $A(x)_k$, where k stands for either TE or TM, such that their integrals are the same. This is done to take out the dependence on overall absorption probability, which is not measured in p_1.
- For each wavelength, compute $j_{th}(x) = j_0 - \gamma(x)E$. We take j_0 to be $j_{c,exp}$, in accordance with the theoretical predictions of the vortex crossing model.
- For each current, for each wavelength, compute the detection probability density $P(X) = \min\{1, \exp(j_b - j_{th})/j^\star\}$, with $j^\star = 0.9$ GA/m^2.
- Compute $p_{1,k}(I, E) = \int_{-w/2}^{w/2} P(x, I, E)A(x)_k dx$.
- Compute the average value of $p_1 = (p_{1,\parallel} + p_{1,\perp})/2$
- Compute the visibility$\mathrm{V}_{I,E} = (p_{1,\parallel} - p_{1,\perp})/(p_{1,\parallel} + p_{1,\perp})$.

In order to fit the internal theshold current profile to the experimental data, we use Tikhonov regularization [98]. That is, to the usual function that is minimized in an inversion problem

$$g(x) = \sum_i (V_i(\gamma'(x)) - V_{i,exp})^2/\sigma_i^2, \tag{5.9}$$

where V is the observed visibility and σ is the error on each visibility, we add the extra term

$$g(x) = \sum_i (V_i(\gamma'(x)) - V_{i,exp})^2/\sigma_i^2 + s\sum_j (\gamma'(x_j) - \gamma'(x_{j+1}))^2, \tag{5.10}$$

which has the effect of penalizing solutions where the difference between adjacent points in the curve is large. This is a standard way of regularizing (i.e. making invertible) nearly ill-posed problems. We apply only weak regularization such that the contribution to $g(x)$ from the second term is approximately 20% of the first. Furthermore, we apply the constraint that the sum $\gamma'(x)$ should be comparable to the sum of the theoretical $\gamma'(x)$ curve. We find that we can fit our data if we set $\sum_i \gamma'(x)_{exp}\Delta x_i$=1.15$\sum_i \gamma'(x)_{theo}\Delta x_i$. We varied the number of points and value of s and verified that the solution presented in the main text is robust.

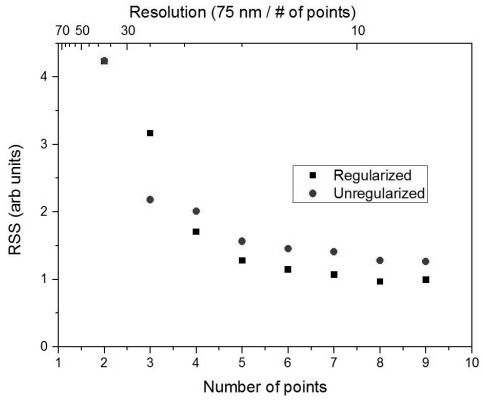

Figure 5.14: Residual sum of squares as a function of the number of points at which we define $\gamma'(x)$, i.e. the number of free parameters in our fit. We observe that beyond $\Delta x = 15$ nm, there is only a slow decrease in our goodness-of-fit parameter. This decrease stops at $\Delta x = 10$ nm. From this, we conclude that the resolution with which we can determine the local IDE is around 10 nm.

5.i.6 Resolution

In this section we will justify the resolution claimed in the main text of Chapter 5. To find the resolution with which we can reconstruct the local IDE, we perform the procedure outlined in section 5.6.5 for various spacings Δx of the points at which we specify $\gamma'(x)$. We define the resolution as that spacing beyond which adding further points does not improve the fit to our experimental data.

In Figure 5.14, we show the results of this procedure. We plot the RSS (residual sum of squares) for both the unregularized and regularized version of our fit (i.e. equations 5.9 and 5.10, respectively). We find (as expected) that the RSS of the regularized fit typically lies above that of the unregularized fit. We find that the value of the RSS decreases rapidly when increasing the number of fit parameters, dropping to 1.3 (in arbitrary units) at a value of $\Delta x = 15$ nm. At $\Delta x = 9.3$ nm, the unregularized RSS reaches a minimum of 0.96. From this, we conclude that the resolution with which we can determine the local IDE is in the range of 10 nm. In Figure 5.15, we show the corresponding fits to our experimental data, for a few representative values of Δx. It can be seen that the fits at high values of Δx do not fit the data. Around $\Delta x = 10$ nm, we achieve a good fit.

We conclude with two remarks. First, as can be seen from the top panel of Figure 5.4, the accuracy with which we can determine the values of $\gamma'(x)$ is higher at the edges of the wire than in the center. The reason for this is that

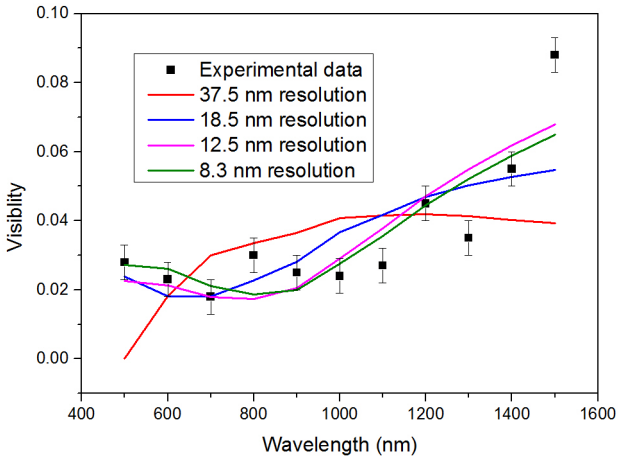

Figure 5.15: Fits of the regularized detection model to our experimental data, for various values of Δx.

the edges contribute much more to the effect of a polarization-dependent internal detection efficency, as these parts are preferentially excited by one polarization. In the discussion above, we have largely assumed a constant spacing between points. In principle, however, the resolution could also be a function of the position along the wire. Our data is not of sufficient quality to say anything quantitative about this, but we expect that the resolution in the center would be lower than at the edges.

Second, we note that our experimental data has several outliers, which are fitted by none of the models. For a model which completely describes the data, we would be able to compute χ^2 to determine which model describes the data with the minimum number of free parameters. Unfortunately, the presence of these outliers precludes this route since we would have $\chi^2 \gg 1$.

5.i.7 Detection Probability Profiles

For completeness, we present all position-dependent quantities in our analysis combined, for three representative wavelengths. In Figures 5.16-5.18, we plot the absorption for both polarizations $A(x)$, internal detection probability $P(x)$ and the detection probability density $P(x)A(x)$ (dashed line) for 1500 nm (Figure 5.16), 1000 nm (Figure 5.17) and 500 nm (Figure 5.18). These graphs clearly illustrate why the visibility of our observed effect increases with wavelength: for short wavelengths, the difference between the two optical absorption probability densities is very small, and occurs only at the outermost 10 nm or so. In contrast, at high wavelengths the difference in

absorption probabilities is much larger, which makes the internal probability distribution more visible.

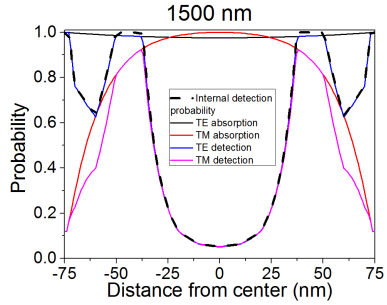

Figure 5.16: Internal detection probability, TE and TM absorption, and TE and TM detection probabilty, for 1500 nm illumination.

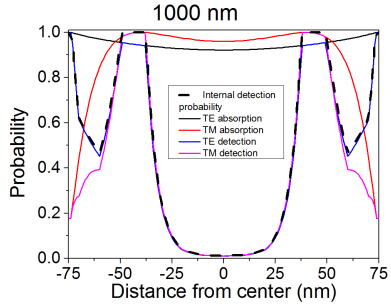

Figure 5.17: Internal detection probability, TE and TM absorption, and TE and TM detection probabilty, for 1000 nm illumination.

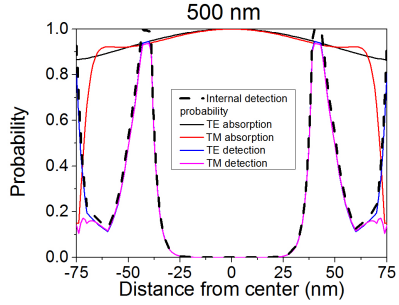

Figure 5.18: Internal detection probability, TE and TM absorption, and TE and TM detection probabilty, for 500 nm illumination.

5.ii Appendix: Implications of the Position Dependence of the Threshold Current of SSPDs

Nanowire superconducting single-photon detectors [1] are a crucial resource for high-efficiency, low-dark count photodetection in the infrared [3]. Such detectors are of great value for many applications, including cancer research [91], and a variety of fundamental experiments [59]. The detection mechanism of such devices is an ongoing field of study which has seen great steps in recent years [17, 24, 25, 28, 32, 33, 34, 35, 72], in part driven by the development of SSPDs made of novel materials such as MoGe [99], WSi [55], MoSi [100] and MgB_2 [101]. The current understanding is that when a photon is absorbed, a cloud of quasiparticles is formed, which diverts the current from the absorption spot. If the current is large enough, a vortex unbinds from the edge of the wire, causing a detection event.

One crucial step in the theoretical understanding was the suggestion that the threshold current of the detector, i.e. the current at which the detector becomes fully efficient, is dependent on the position along the cross-section of the wire [34, 32] where the photon is absorbed. In Chapter 5, we demonstrated a measurement of this position-dependent threshold current via a differential measurement of two absorption probability profiles induced by parallel and orthogonal polarization. This confirmed an earlier preliminary result by Anant *et al.* [10] of a position-dependent internal threshold current. Within our model, the position-dependent detection efficiency is explained by the fact that vortices enter more easily at the point where superconductivity is already weakened by the presence of quasiparticles.

We demonstrated a reconstruction of this internal threshold current with a resolution around 10 nm. This is shown in Figure 5.19, where we plot the final result from Chapter 5. We plot the position-dependent detection efficiency as established from our experiments, as well as a theoretical calculation done in the vortex crossing model.

In this Appendix, we discuss the implications of a position-dependent threshold current on other quantities which have been used to investigate the detection mechanism. We take the result in Figure 5.17 as a point of departure for our calculations. We will focus on two of them: the universal curve of the detection probability and the energy-current relation. We first review the main ingredients of our model. We then move on to discuss the implications for the two quantities mentioned above.

5.ii.1 Ingredients of the Model

Our model of detection events in superconducting single-photon detectors is inspired by previous experimental observations reported in Chapters 3 and 4 and by the numerical simulations described in [28, 32]. In these experiments, we found that the threshold current required to achieve a constant detection

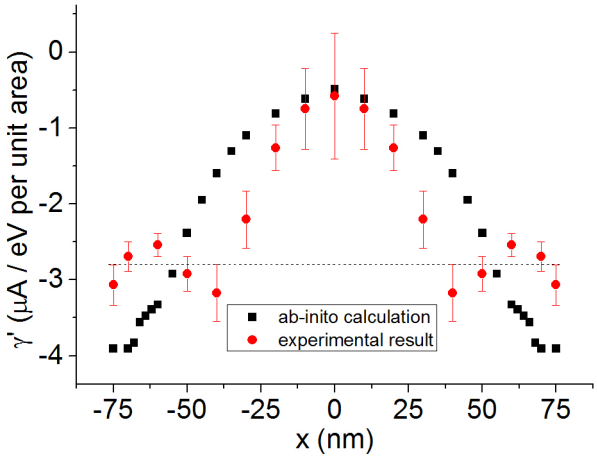

Figure 5.19: Position dependent threshold current slope in a 150 nm wide NbN SSPD. We have converted γ'(x) to macroscopic units for easy comparison with other experimental data. The dashed line shows the threshold current which is observed for the entire wire, at low detection probabilities.

probability $I_{th} = I_0 - \gamma E$, where E is the photon energy, γ is a conversion constant - which was found to be width-dependent - and I_0 is a current scale, which was found to be $I_0 \approx 0.8 I_c$ for a 1% detection probability at T = 3.1 K on a 220 nm wide nanodetector [17].

The numerical simulations consist of a series calculations of the threshold current as a function of photon energy and absorption position. From these calculations, we find that the linear energy-current relation extends microscopically as well, that is: $j_{th} = j_0 - \gamma'(x)E$. In this way, we introduce a position-dependent threshold current. We found in Chapter 5, however, that in order to make our calculations agree with the observed experimental data, we had to make a fit which resulted in slightly different values for $\gamma'(x)$ than were predicted by theory.

A second component of our detection model is the assumption that the detection probability decreases exponentially below the threshold current: $P(x) = \min\{1, \exp((j_b - j_{th})/j^\star)\}$, where I_b is the applied bias current, j_{th} is the threshold current calculated from the local energy-current relation and $j^\star$ is a current scale that describes the detection probability below threshold. $j^\star$ is in principle an unknown quantity, but it can easily be read off from the current dependence of the detection probability at very low current. This proposed expression is justified by the notion that low-detection probability detection events are a tunneling process, similar to dark counts. Around $I_b = I_c$, the relation between bias current and energy barrier is linear [24].

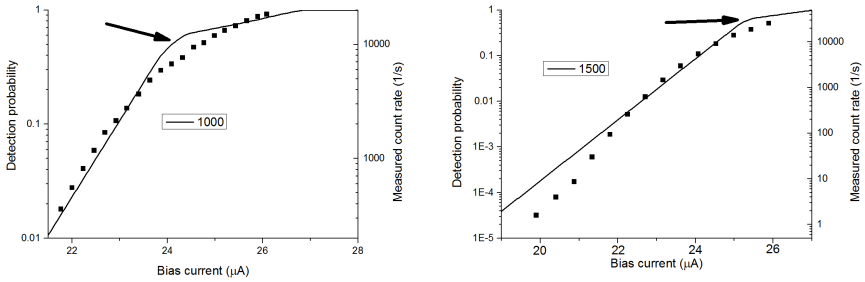

Figure 5.20: Computed versus observed detection probability as a function of bias current for 1000 nm and 1500 nm. The squares show experimental data, and the solid lines show a detection probability computed as described in the main text. The arrows indicate the point where the first sections of the wire become fully photodetecting.

This serves as justification of our proposed relation.

With these two ingredients, we can calculate the internal detection probability p_1 as a function of bias current: we first compute j_{th} for the photon energy we are interested in, then compute the local detection probability. We then compute the integral $p_1 = \int_{-w/2}^{w/2} P(x)A(x)dx$, where $A(x)$ is the absorption probability as a function of position.

We show the results of this computation in Figure 5.20 for two different wavelengths. We note that our calculated curves coincide with the experimental data to within a factor of 2 while the measured count rate changes over 2-4 orders of magnitude. Moreover, we note that the efficiency implied by these measurements ($\eta \approx 10^{-5}$) is in good agreement with the geometry of our experiment, in which a free-space beam of a few tens of μm is impinging on a 100 nm x 150 nm active area. We therefore conclude that our calculations are in reasonable agreement with our measurements.

5.ii.2 Universal Curve

In Chapter 3, the idea was put forward that there is a universal curve for photodetection in SSPDs. We observed that for photons with a wavelength between 1000 nm and 1500 nm, the detection probability as a function of bias current superimposes when they are rescaled as $p_1(I, E) = p_1(I - \gamma E)$. In this section, we will demonstrate that this is only approximately true: this relation holds only for photon states with sufficiently low energy or for sufficiently low detection probability.

Figure 5.21 shows the calculated detection probability for various wavelengths, calculated in the way described in Section 5.7.2. We clearly observe three regimes: a regime where the detection probability increases exponentially with

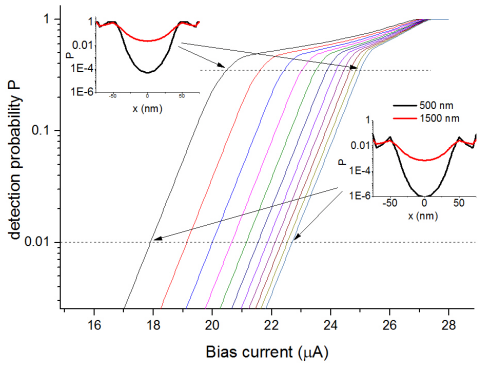

Figure 5.21: Computed detection probability as a function of bias current and photon energy, for wavelengths from 500 nm (leftmost curve) to 1500 nm (rightmost curve). *Insets:* Detection probability distribution for two wavelengths, at constant overall detection probability.

applied bias current, a regime where the detection probability increases, but much more slowly, and a regime where the detection probability is saturated at unity. These three regimes correspond to what is observed in experiments [8]. With these results, we can therefore offer an explanation of these three regimes.

In the low-detection probability regime, only the edges of the detector are photodetecting, and with low probability (see right inset of Figure 5.21). As the current is increased, gradually the edges become more efficient. Eventually, the edges of the detector saturate (see left inset of Figure 5.21) and we enter the second regime. In this regime of slowly increasing detection probability, the detection probability is increased because the area which is fully photodetecting moves inward. Eventually, the third regime is reached where the entire detector is operating with probability unity and the internal detection efficiency is constant. This result provides an explanation for the slow roll-off of the detection efficiency at low bias currents, which was previously attributed to inhomogeneities in the detector. We note that our explanation was put forward independently by Zotova and Vodolazov [34].

5.ii.3 Threshold Current

Measurements of the energy-current relation are a common way of investigating the detection mechanism [8, 16, 17, 35, 20, 73, 72]. The procedure is to take various excitation energies and bias currents and observe the iso-detection probabiltiy lines, i.e. those combinations of bias current and photon energy for which a particular predefined threshold detection probab-

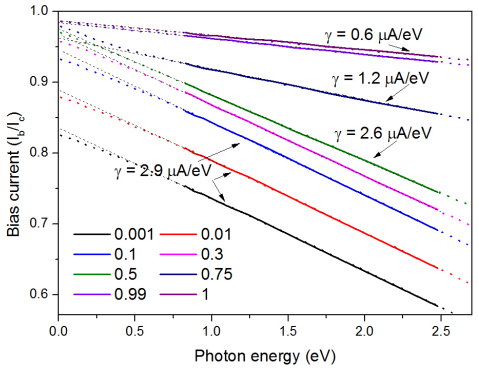

Figure 5.22: Calculated curves of constant overall detection probability for various threshold probability levels for a 150 nm wide detector. The solid lines indicate the wavelength range over which the experiment in Chapter 5 was conducted. The dashed lines indicate linear extrapolation to lower currents; the dotted lines indicate the computed theshold current at lower photon energies. The arrows and captions indicate the macroscopic values of γ found at these threshold values.

ility is achieved. Usual values are 1% to 10%. Also in use is an empirical rolloff-formula which is equivalent to a detection probability of 50% [73].

In Figure 5.22, we plot a series of computed energy-current relations. From this figure, we conclude that the energy-current relation depends on the choice of threshold criterion. However, below a threshold criterion of $p_1 = 0.3$ this dependence is very weak. This is consistent with our observations at low detection probabilities, where we observed no effect of changing the threshold criterion on the measured value of γ.

We observe that the point at which the threshold current intercepts the y-axis when extrapolated to zero energy is smaller than I_c. To compute these graphs we used a value of $I_0 = I_c$, in the threshold current formula $I_{th} = I_0 - \gamma E$, but our extrapolated values of I_0 are lower than I_c. This resolves an important discrepancy between experimental results and theory. In theoretical work, the current at which vortex crossings are possible is identified as the experimental critical current, whereas experimentally, $I_0 \approx 0.8 I_{c,exp}$ was found at T = 3.1 K. Our computation demonstrates that both are true at the same time: the position-dependence of the detection efficiency gives rise to an effective value of I_0 that is lower than its actual value.

This effect is due to the fact that, at high photon energies, the detection probability is set almost exclusively by the single point which is most strongly photodetecting. As the photon energy is decreased, however, other parts of the wire start to participate. This means that the detection probability

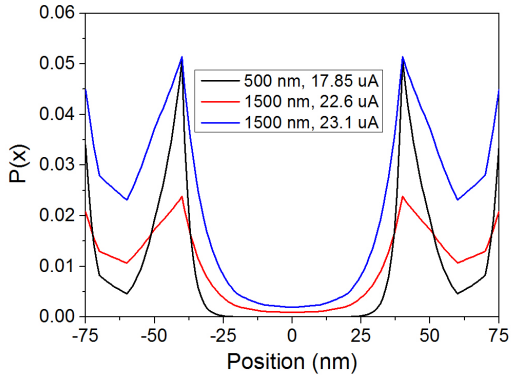

Figure 5.23: Internal detection probability for three combinations of bias currents and photon wavelengths. This figure illustrates why the overall $\gamma(x)$ measured in macroscopic experiments is smaller than the maximum value of $\gamma'(x)$. The black curve shows the detection probabilty profile that has an overall detection probabilty of 1% for light with $\lambda = 500$ nm. The red curve shows the equivalent curve for light with $\lambda = 1500$ nm. The blue curve shows the detection probability for $\lambda = 1500$ at the current at which the most strongly photodetecting point is equally efficient as in the case of 1% detection probability at 500 nm. In this last case, the overall photodetection probability is 2.2%.

in the most strongly photodetecting point in the wire actually becomes less when we go to lower photon energies and higher currents, keeping the overall detection probability constant.

Effectively, the macroscopic γ which is measured is a weighted average of the $\gamma'(x)$ curve, where obviously points with high detection probability count more strongly. This can be seen by comparing Figures 5.17 and 5.20; the value of $\gamma'(x)$ has its maximum at $\gamma'(40\text{ nm}) = 3.2\ \mu$A/eV but the wire as a whole has $\gamma = 2.9\ \mu$A/eV. This effect is illustrated in Figure 5.23, where the internal detection probability is plotted for a number of combinations of photon energy and bias current which all satisfy the 1% detection probability criterion.

The dashed lines in Figure 5.22 show computed threshold currents at very low values of excitation energy. At low values of excitation energy, the linear relation between bias current and photon energy breaks down. The detection probability at $E = 0$ has an exponential dependence on the threshold current $R(I, E = 0) \propto \exp(I_b - I_c)$. It is tempting to think that in this way, we have naturally accounted for dark counts in our model. However, experimentally we find that the extrapolated values of our linear energy-current relation are

far away from the currents at which we observe any dark counts[15]. E.g. for the device presented in Chapter 4, we find $I_0 = 33.8\ \mu$A, for a threshold value of $p_1 = 0.01$, whereas we don't observe any dark counts until we approach the critical current $I_c = 44\mu$A. We therefore conclude that this effect represents at best a partial solution of the dark count problem: the assumption that dark counts can be understood as photon counts at energy $E = 0$ is a natural feature of the kind of model which we present here, but is in disagreement with experimental data.

[15] See Chapters 3 & 4.